frontiers | Frontiers in Chemistry

TYPE Original Research
PUBLISHED 26 September 2024
DOI 10.3389/fchem.2024.1475131



OPEN ACCESS

EDITED BY
Yang Liu,
Nanyang Technological University, Singapore

REVIEWED BY
Zixin Wang,
Los Alamos National Laboratory (DOE), United States
Xiao-Jing He,
The Second Affiliated Hospital of Chongqing Medical University, China

*CORRESPONDENCE
Qinghe Han,
hanqinghe@mails.jlu.edu.cn
Qinghai Yuan,
yuanqinghai123@sina.com

RECEIVED 02 August 2024
ACCEPTED 11 September 2024
PUBLISHED 26 September 2024

CITATION
Ma R, Zhang P, Chen X, Zhang M, Han Q and Yuan Q (2024) Dual-responsive nanoplatform for integrated cancer diagnosis and therapy: Unleashing the power of tumor microenvironment.
*Front. Chem.* 12:1475131.
doi: 10.3389/fchem.2024.1475131



# Dual-responsive nanoplatform for integrated cancer diagnosis and therapy: Unleashing the power of tumor microenvironment

Rui Ma, Peng Zhang, Xiuying Chen, Mengdi Zhang, Qinghe Han* and Qinghai Yuan*

Department of Radiology, The Second Hospital of Jilin University, Changchun, China

Chemodynamic therapy (CDT), designed to trigger a tumor-specific hydrogen peroxide ($H_2O_2$) reaction generating highly toxic hydroxyl radicals (·OH), has been investigated for cancer treatment. Unfortunately, the limited Fenton or Fenton-like reaction rate and the significant impact of excessive reducing glutathione (GSH) in the tumor microenvironment (TME) have severely compromised the effectiveness of CDT. To address this issue, we designed a dual-responsive nanoplatform utilizing a metal-polyphenol network (MPN) -coated multi-caged $IrO_x$ for efficient anti-tumor therapy in response to the acidic TME and intracellular excess of GSH, in which MPN composed of $Fe^{3+}$ and tannic acid (TA). Initially, the acidic TME and intracellular excess of GSH lead to the degradation of the MPN shell, resulting in the release of $Fe^{3+}$ and exposure of the $IrO_x$ core, facilitating the efficient dual-pathway CDT. Subsequently, the nanoplatform can mitigate the attenuation of CDT by consuming the excessive GSH within the tumor. Finally, the multi-caged structure of $IrO_x$ is advantageous for effectively implementing photothermal therapy (PTT) in coordination with CDT, further enhancing the therapeutic efficacy of tumors. Moreover, the outstanding Computed Tomography (CT) and Magnetic Resonance Imaging (MRI) ($T_1/T_2$) multimodal imaging capabilities of $IrO_x$@MPN enable early diagnosis and timely treatment. This work provides a typical example of the construction of a novel multifunctional platform for dual-responsive treatment of tumors.

KEYWORDS

**metal-polyphenol network, computed tomography, magnetic resonance imaging, chemodynamic therapy, photothermal therapy**

## 1 Introduction

CDT utilizes the endogenous $H_2O_2$ that existed in the TME to produce· OH (Liu et al., 2023; Zou et al., 2022; Lin et al., 2020). Fenton or Fenton-like reactions encompass a class of processes where $Fe^{3+}$, iron-containing minerals, and other transition metal ions can either accelerate or substitute for $Fe^{2+}$ in catalyzing the decomposition of $H_2O_2$ (Jana and Zhao, 2022; Zhang et al., 2022; Zheng et al., 2022; Getachew et al., 2021). The ·OH formed can compromise tumor cells by causing lipid peroxidation, inactivating proteins, and inflicting DNA damage, which in turn induces oxidative stress and promotes cell death (Meng et al., 2020). Unlike other treatment approaches, CDT is specifically triggered by internal

biological signals, which enhances its selectivity and makes it a highly targeted therapeutic strategy (Tang et al., 2021). Additionally, it exhibits high sensitivity to various factors in the TME, including catalytic ion concentration and multiple factors such as $H_2O_2$, GSH, and pH values. Despite its considerable promise, CDT as a sole therapeutic approach faces limitations due to the scarcity of endogenous $H_2O_2$ in the tumor environment and the decreased effectiveness of Fenton or Fenton-like reactions in the mildly acidic pH range of 5.6–6.8. Simultaneously, the GSH-mediated cellular antioxidant defense system (ADS) can eliminate reactive oxygen species (ROS) within cells, significantly reducing the ·OH production rate and the therapeutic efficiency of CDT (Lin et al., 2019; Wang Z. et al., 2019; Hao et al., 2020). Therefore, depleting GSH to overcome the protective effect of ADS is crucial for enhancing the CDT effect. Moreover, achieving optimal therapeutic results with CDT alone is challenging due to the complexity, diversity, and variability within the TME. Currently, combined cancer therapy has emerged and undergone in-depth research, significantly improving treatment effectiveness while minimizing adverse reactions (Jiang et al., 2021; Manivasagan et al., 2022; Feng et al., 2021). Among various combination cancer treatments, the pairing of PTT with CDT stands out as a highly promising approach, offering superior selectivity, reduced toxicity, and minimal invasiveness (Manivasagan et al., 2022; Feng et al., 2021). PTT harnesses light absorption by photothermal agents to generate localized heat or induce thermal ablation, effectively targeting and destroying cancer cells (Li et al., 2020). Research has shown that increasing the temperature within the tumor site can notably improve the effectiveness of Fenton or Fenton-like reactions, thus accelerating the generation of ·OH radicals (Wang et al., 2020; Wang X. et al., 2019). Therefore, the exploration of a highly efficient nanoplatform for combined CDT/PTT to maximize the antitumor effect represents an attractive research direction (Liu et al., 2019; Huang et al., 2017; Abbas et al., 2017; Liu et al., 2018).

The nanoplatforms composed of iridium (Ir) have sparked widespread interest among researchers across various fields due to their unique optical and physical properties (Yin et al., 2021; Shen et al., 2021). On one hand, it has been shown to exhibit robust catalase activity for oxygen evolution across a diverse range of pH levels (An and Tc, 2002; Yip and Lo, 2018). On the other hand, Ir-based complexes are distinguished by their superior photothermal conversion capabilities, impressive photostability, and low levels of cytotoxicity (Zhen et al., 2020a; Zhen et al., 2020b; Zhen et al., 2018). Furthermore, due to the significant atomic number (Z = 77) and robust nature of the transition metal Ir element, $IrO_x$ exhibits excellent X-ray absorption capability and can be employed for CT imaging (Zhen et al., 2020b). Based on the characteristics mentioned above, Ir-based nanomaterials could be employed for CDT and PTT of tumors, achieving promising therapeutic outcomes (Deng et al., 2022; Nie et al., 2022). While Ir-based nanomaterials hold tremendous potential, their standalone catalysis in initiating Fenton-like reactions is limited and cannot overcome the constraints of the ADS system. Therefore, it is necessary to explore functionalized Ir-based nanomaterials to meet these requirements.

Herein, we developed a core-shell nanoplatform ($IrO_x$@MPN) that is responsive to both the acidic TME and GSH for combined CDT/PTT and CT/MRI imaging of tumors. This nanoplatform based on $IrO_x$ is coated by the metal-polyphenol network (MPN) and features $Fe^{3+}$ and tannic acid (TA) coating on multi-caged $IrO_x$ nanoparticles, to achieve integrated diagnosis and treatment. MPN, consisting of $Fe^{3+}$ and tannic acid (TA), possesses pH-responsiveness, as polyphenols readily dissociate from metal ions in low pH environments (Liu et al., 2023), allowing for controlled release of $Fe^{3+}$. Moreover, MPN could dissociate under intracellular stimuli, such as adenosine triphosphate (ATP) and GSH (Peng et al., 2022), thus exposing the $IrO_x$ core. The $IrO_x$ core exhibits intrinsic activities similar to catalase and peroxidase, enabling the conversion of excessive $H_2O_2$ in the tumor tissue into oxygen ($O_2$) and generating ·OH. Moreover, the self-cyclic valence alternation between $Ir^{4+}$ and $Ir^{3+}$ allows $IrO_x$ to continuously consume GSH, alleviating tumor hypoxia and improving antioxidant capacity. Simultaneously, $Fe^{3+}$ can be reduced to $Fe^{2+}$ by TA and GSH, and $Fe^{2+}$ exhibits catalytic performance, reacting with the $H_2O_2$ presented in the TME to generate ·OH through Fenton reactions. The released $Fe^{3+}$ can further deplete GSH, enhancing the CDT effect. The multi-caged structure of $IrO_x$ could enhance the photothermal effect and loading capacity (Zhen et al., 2018), resulting in high photothermal conversion efficiency (60.78%). Due to the coordination of polyphenols with $Fe^{3+}$ ions in MPN (Liu et al., 2023; Cen et al., 2023; Wang et al., 2022; Spinello et al., 2016; Guo et al., 2014), the nanoplatform also possesses a pH-activated enhancement of $T_1$-$T_2$ dual-modal imaging capability in the TME. Additionally, the $IrO_x$ core exhibited excellent CT imaging capability. Therefore, $IrO_x$@MPN represents a promising dual-responsive CDT/PTT multifunctional nanoplatform with concurrent CT and MRI multimodal imaging capabilities.

# 2 Materials and methods

## 2.1 Materials

Iridium trichloride (99.99%, metal basis), 1,3-diphenylisobenzofuran (DPBF), Methylene blue (MB), 1,10-phenanthroline, sodium hydroxide (NaOH), calcein acetoxymethyl ester (Calcein AM), propidium iodide (PI) was sourced from Aladdin Reagent Co. (Shanghai, China). 5, 50-dithiobis (2-nitrobenzoic acid) (DTNB), ethanol, hydrogen peroxide ($H_2O_2$, 30%), [Ru (dpp)$_3$]$Cl_2$ (RuDPP), 2,7-dichlorofluorescin diacetate (DCFH-DA), Fluorescein Isothiocyanate Isomer I (FITC), dimethyl sulfoxide (DMSO) was obtained from Sigma-Aldrich (America). Hematoxylin-eosin (H&E), and Dulbecco's modified eagle's medium (DMEM) were acquired from Thermo Scientific Co. (Beijing, China). Throughout the experiments, deionized (D.I.) water was used exclusively. All chemicals were used directly as provided, without any additional purification steps.

## 2.2 Characterizations

Transmission electron microscopy imaging was performed with FEI TECNAI G2 F20. The UV-visible absorption spectra were recorded by Hitachi U-3100 spectrophotometer. X-ray photoelectron spectroscopy was conducted with an

ESCALab220i-XL electron spectrometer. The binding energies for all analyzed elements were referenced to the C 1s peak of adventitious carbon, with the energy fixed at 284.6 eV. The content of Ir and Fe elements was determined using ICP-OES (Thermo Fisher Scientific, United States). The dissolved oxygen content was assessed with a portable dissolved oxygen meter (JPBJ-608) from Shanghai Instrument Scientific Instrument Co., Ltd., China. Fluorescence images of cells were captured with a Leica TCS SP2 confocal laser scanning microscope. The pH value was obtained using a pH meter (PB-10) from Sartorius, Germany.

## 2.3 Preparation of multi-caged $IrO_x$

$IrCl_3{\cdot}6H_2O$ (0.1493 g) was dissolved in 50 mL of water and allowed to be stirred for 3 h. The solution was then kept at 4°C for about 3 days until it cleared. Then, the $IrCl_3$ aqueous solution was kept at room temperature for ~2 h. Next, a 1.0 M NaOH solution was slowly added to bring the pH to 12. The mixture was then continuously stirred at room temperature for an additional 2.5 h. Afterward, it was transferred to an oil bath, where vigorous stirring was maintained as the temperature was raised to 80°C. The oil temperature could rise to 80°C within 25 min. The reaction was continued for 13 h under conditions that facilitated condensation. The $IrO_x$ nanoparticles were subsequently isolated by spinning at 15,000 rpm for 10 min, then thoroughly washed with ethanol and water before being prepared for further use. The collected nanoparticles were freeze-dried and stored for later applications.

## 2.4 Preparation of multi-caged $IrO_x$@MPN

$IrO_x$ NPs (8 mL, 4 mM) were placed into a 10 mL centrifuge tube. 40 μL of TA (40.8 mg/mL) was added to the $IrO_x$ NPs for 20 s. Next, 40 μL of $FeCl_3$ (48 mM) was added. Next, 2 mL of Tris buffer (50 mM, pH 8.0) was introduced, followed by blending the mixture for 20 s. The solution was subsequently spun at 12,000 rpm for 10 min, followed by two washings with $ddH_2O$ to isolate $IrO_x$@MPN. The concentrations of Ir and Fe in the prepared $IrO_x$@MPN were measured to be 307.3 and 6.7 μg/mL by ICP-OES, respectively. $IrO_x$@MPN with different Ir/Fe ratios were synthesized using the same procedure, with the exception of altering the concentration of $FeCl_3$.

## 2.5 Preparation of Fluorescein Isothiocyanate Isomer I-conjugated $IrO_x$@MPN ($IrO_x$@MPN-FITC)

To investigate the intracellular uptake of $IrO_x$@MPN, Fluorescein Isothiocyanate Isomer I (FITC)-loaded $IrO_x$@MPN was prepared. Firstly, 500 μg of FITC was combined with 1 mL of dimethyl sulfoxide (DMSO) and mixed at room temperature for 1 h. Next, 1 mL of $IrO_x$@MPN solution in deionized water (2.5 mg/mL) was introduced and stirred overnight. The product was thoroughly rinsed with deionized water until the supernatant was almost completely clear.

## 2.6 Extracellular $Fe^{2+}$ generation

Reduced $Fe^{2+}$ was detected using 1,10-phenanthrolin. 1 mg of $IrO_x$@MPN, with or without GSH (10 mM), was suspended in 1 mL of aqueous solution at pH 7.4 or 5.0 and stirred for 1 h. Subsequently, 1 mL of 1,10-phenanthroline ethanol solution (1 mg/mL) was combined with 1 mL of $IrO_x$@MPN aqueous solution, with or without GSH, and the mixture was left to sit for 10 min. Absorbance was then assessed at 508 nm with UV-Vis spectrophotometry. For comparison, UV-Vis spectra of 1,10-phenanthroline alone were also recorded.

## 2.7 Extracellular $O_2$ generation

Oxygen generation was monitored with a dissolved oxygen (DO) meter. Generally, 29.7 mL of $IrO_x$@MPN solution (Ir concentrations: 0.5 mM) was combined with 300 μL of $H_2O_2$ solution (100 μM) while stirring vigorously. The changes in dissolved oxygen were automatically recorded at 10s intervals. All the solutions were pre-saturated with $N_2$ until the dissolved oxygen was 0%. As controls, the generated $O_2$ of $H_2O$, $H_2O_2$, and $IrO_x$/$H_2O_2$, were also monitored for comparison.

## 2.8 Extracellular ·OH generation

·OH was detected using methylene blue (MB). Firstly, $IrO_x$@MPN (Ir concentration: 100 μg/mL) was incubated with aqueous solutions (pH = 7.4 or 5.0) with or without GSH (1 mM) for 3 h. Next, MB aqueous solution (3 mL, 10 mg/L), $H_2O_2$ (100 μM), and $IrO_x$@MPN aqueous solutions were thoroughly mixed, followed by centrifugation to collect the supernatant. Absorption around 660 nm was subsequently measured using UV-Vis spectroscopy. The variations in MB absorption in different groups were similarly assessed following the same procedures, including MB, MB/$H_2O_2$, MB/$IrO_x$, MB/$IrO_x$@MPN, MB/$IrO_x$@MPN/GSH, MB/$IrO_x$@MPN/$H^+$, MB/$IrO_x$@MPN/$H_2O_2$, MB/$IrO_x$@MPN/GSH/$H_2O_2$, MB/$IrO_x$@MPN/$H^+$/$H_2O_2$, and MB/$IrO_x$@MPN/$H^+$/GSH/$H_2O_2$.

## 2.9 Extracellular GSH depletion

The GSH level was investigated by utilizing 5, 50-dithiobis (2-nitrobenzoic acid) (DTNB). GSH aqueous solution (1 mM) was added into $IrO_x$ and $IrO_x$@MPN aqueous solution (50 μg/mL). DTNB PBS solution (1.5 mg/mL) was added into $IrO_x$@MPN aqueous solution after different reaction times, and the absorbance of the mixture was then analyzed using a UV-Vis spectrophotometer.

## 2.10 Photothermal of $IrO_x$@MPN

1 mL of $IrO_x$@MPN PBS solutions with varying Ir concentrations (0, 0.125, 0.25, 0.5, 1 mg/mL) were subjected to an 808 nm laser with an intensity of 1 W/cm$^2$ for 10 min, The

temperature of these solutions was tracked using a thermocouple probe, and measurements were taken every 30 s. Additionally, to evaluate the thermal stability of $IrO_x$@MPN, an aqueous solution of $IrO_x$@MPN (0.5 mg/mL) was subjected to an 808 nm laser with an intensity of 1 W/cm$^2$ for 10 min in a quartz cuvette, and the temperature was lowered down through natural cooling, repeated the above steps for five times.

## 2.11 Incubation of cells

Mouse breast cancer cells (4T1) and mouse fibroblasts (L929) were provided by the Institute of Biochemistry and Cell Biology, Chinese Academy of Sciences. 4T1 and L929 cells were grown in DMEM medium ([glucose] = 4.5 g/L) enriched with 10% fetal bovine serum (FBS), penicillin (100 units/mL), and streptomycin (100 μg/mL). The cells were plated at a concentration of $10^6$ cells per 25 cm$^2$ flask and incubated at 37°C in a 5% $CO_2$ environment for 24 h.

## 2.12 *In Vitro* cytotoxicity study

The 96-well plates were seeded with L929 and 4T1 cells at a density of $5 \times 10^3$ cells per well and incubated for 24 h. Each well received 100 μL of $IrO_x$@MPN medium solutions with concentrations of 0, 13, 25, 50, 100, and 200 μg/mL, and was then incubated for an extra 24 h. Subsequently, the cells were rinsed three times with PBS, after which 100 μL of CCK-8 DMEM solution (CCK-8: DMEM = 1:10) was added. The cells were further cultured for 1 h. Cell viability was determined by analyzing the absorbance at 450 nm with a microplate reader.

## 2.13 Cellular uptake of $IrO_x$@MPN

Cells of the 4T1 line were introduced into a 6-well culture plate and maintained in a 37°C environment with 5% $CO_2$ for a duration of 24 h, Subsequently, the cells were exposed to $IrO_x$@MPN-FITC for various durations, specifically 30 min, 1 h, 2 h, and 4 h. Then, the cells were subjected to two washes with PBS and then stained with Hoechst 33,342. The cellular uptake was observed using an intracellular fluorescence microscope.

## 2.14 Intracellular GSH consumption

Cells of the 4T1 line were introduced into a 6-well culture plate and maintained in a 37°C environment with 5% $CO_2$ for a duration of 24 h. Then, the cells were further incubated with $IrO_x$ and $IrO_x$@MPN medium solutions (50 μg/mL) for 24 h. Subsequently, each well was rinsed with PBS three times, and the cells were harvested and centrifuged at 3,000 rpm for 10 min. Then, cells were disrupted by RIPA Lysis buffer for 5 min and re-suspended in 500 μL of PBS. An equal volume of 100 μL cell lysate and reagent 1) from the assay kit were mixed and subjected to centrifugation at 3,500 rpm for 10 min. Following centrifugation, 100 μL of the resulting supernatant was combined with 100 μL of reagent 2) and 25 μL of reagent 3). The absorbance at 420 nm was subsequently recorded using UV-Vis spectroscopy. A UV-Vis absorption spectrum of a GSH standard sample (20 μmol/L) was recorded for comparison.

## 2.15 Intracellular $O_2$ generation

$[(Ru(dpp)_3)]Cl_2$ was employed as the $O_2$ sensing probe. 4T1 cells were seeded into a 96-well plate and incubated under the same conditions as previously used for cell culture. Next, a 5 μM solution of $[(Ru(dpp)_3)]Cl_2$ was added to the cells and left for incubation over 4 h. Following this, the plate was washed with PBS and further incubated with DMEM medium, $IrO_x$ (50 μg/mL in DMEM), $IrO_x$@MPN (50 μg/mL in DMEM) for 4 h. Finally, after washing the cells with PBS, red fluorescence images were captured using an intracellular fluorescence microscope ($\lambda_{ex}$ = 488 nm, $\lambda_{em}$ = 620 nm).

## 2.16 Intracellular ROS production

We detected intracellular ROS using 2,7-dichlorofluorescin diacetate (DCFH-DA) as the probe. 4T1 cells were seeded into a 6-well plate and incubated under the same conditions as previously used for cell culture. Next, the cells were exposed to 10 μM DCFH-DA in DMEM for 20 min. After washing the wells three times with PBS, they were further incubated for 12 h with either 2 mL of DMEM alone, DMEM with 50 μg/mL $IrO_x$, or DMEM with 50 μg/mL $IrO_x$@MPN. After another round of washing with PBS, images were captured using an intracellular fluorescence microscope ($\lambda_{ex}$ = 504 nm, $\lambda_{em}$ = 529 nm).

## 2.17 *In Vitro* chemodynamic therapy

4T1 cells were seeded into a 96-well plate and incubated under the same conditions as previously used for cell culture. They were then treated with either DMEM, a 50 μg/mL $IrO_x$ solution in DMEM, or a 50 μg/mL $IrO_x$@MPN solution in DMEM for 12 h. Following treatment, cell viability was evaluated using an intracellular fluorescence microscope after a 30-min staining with Calcein AM and PI.

## 2.18 *In Vitro* photothermal therapy

After cultivating 4T1 cells in a 96-well plate, they were treated with DMEM, a 50 μg/mL $IrO_x$ solution in DMEM, or a 50 μg/mL $IrO_x$@MPN solution in DMEM for 12 h. Following a PBS wash, the 4T1 cells were exposed to 808 nm laser irradiation at 1.0 W/cm$^2$ for 10 min. Cell viability was then evaluated using an intracellular fluorescence microscope after a 30 min staining with Calcein AM and PI. The efficiency of photothermal conversion (η) was determined using the equations outlined below.

$$\theta = \frac{T - Tsurr_{(sample)}}{T_{max\,(sample)} - T_{surr\,(sample)}}$$

$$t = \tau_s \times (-\ln\theta)$$

$$hS = \frac{m_d \times c_d}{\tau_s}$$

$$Q_{dis} = hS\left(T_{max\,(water)} - T_{surr\,(sample)}\right)$$

$$\eta = \frac{hS\left(T_{max\,(sample)} - T_{surr\,(sample)}\right) - Q_{dis}}{I\left(1 - 10^{A808}\right)}$$

$$hS = \frac{m_d \times c_d}{\tau_s}$$

h ($mWm^{-2}\,°C^{-1}$): Heat transfer coefficient.S ($m^2$): Surface area of the container. $T_{max}$ (°C): Equilibrium temperature. $T_{surr}$ (°C): Ambient temperature of the surroundings. $Q_{Dis}$ (mW): The heat from light absorbed by the quartz cuvette walls itself was measured independently using a quartz cuvette cell containing aqueous samples without NPs.

## 2.19 *In vivo* therapy

All the animal experiments were conducted following the National Regulation of China for Care and Use of Laboratory Animals and approved by the Institutional Animal Care and Use Committee of Changchun Institute of Applied Chemistry, Chinese Academy of Sciences (Grant no. 20230065). *In vivo*, therapy was conducted using a subcutaneous tumor model. Each mouse was injected subcutaneously with 100 μL of a suspension containing $4 \times 10^6$ 4T1 cells into the right hind leg. The tumors were permitted to develop until they reached approximately 100 $mm^3$ in size. Tumor models were established using female Balb/C mice aged 6–8 weeks, following the procedures described above. The mice were allocated into six distinct groups, each consisting of five mice (n = 5). These groups were: 1) control (saline solution injection); 2) Laser; 3) $IrO_x$ (injected with a 100 μL solution of $IrO_x$ at 10 mg/kg); 4) $IrO_x$/Laser; 5) $IrO_x$@MPN (injected with a 100 μL solution of $IrO_x$@MPN at 10 mg/kg); 6) $IrO_x$@MPN/Laser. After intravenous injection of 24 h, the tumors were subjected to 808 nm laser irradiation at 1 W/$cm^2$ for 10 min. Every mice was injected every 2 days. Additionally, tumor dimensions were measured using a digital caliper, and the volume was calculated with the formula: $Volume = (Length \times Width^2)/2$. The relative tumor volume was determined by dividing the post-treatment volume $V$ by the pre-treatment volume $V_0$. Concurrently, the mice's body weight was tracked bi-daily to monitor any long-term toxic effects *in vivo*. On the 15th day, tumors from each treatment group were surgically removed and weighed. Finally, the mice's major organs were excised and preserved in 4% paraformaldehyde for histological analysis. This procedure was aimed at further evaluating the biocompatibility of $IrO_x$ and $IrO_x$@MPN.

## 2.20 *In vitro* and *In vivo* CT imaging

CT images of $IrO_x$@MPN solutions (Ir concentration: 0, 0.25, 0.5, 1, 2, 4, 8, and 16 mg/mL) were measured using CT Scanner. For *in vivo* CT imaging, the tumor-bearing mice were intravenously injected with 100 μL of $IrO_x$@MPN (3 mg/mL in saline). CT scans were performed at different intervals post-injection, specifically at 0 h, 2 h, 24 h, 48 h, and 72 h. Coronal and 3D images were generated using multiplanar reconstruction.

## 2.21 *In vitro* and *In vivo* MRI imaging

MRI images of $IrO_x$@MPN solutions were measured using IngFenia CX 3.0 T MR scanner, with a 32-channel body coil. MR sequences included $T_1$-weighted imaging ($T_1$WI), and $T_2$-weighted imaging ($T_2$WI). The $T_1$ and $T_2$ relaxation time was measured using $IrO_x$@MPN solutions with different Fe concentrations by a workstation (IntelliSpace Portal, Philips Healthcare). To facilitate *in vivo* MRI imaging, once the tumors reached approximately 150 $mm^3$, 100 μL of $IrO_x$@MPN (2 mg/mL in saline) was administered intravenously to the mice, and imaged by the MR scanner, respectively after 0 h (pre-), 2 h, 24 h, 48 h of injection.

## 2.22 blood analysis

Eight mice were divided into two groups to assess blood parameters. In one group, four mice received an intravenous injection of $IrO_x$@MPN at a dosage of 10 mg/kg. On the 30th day, blood samples were drawn from the eye sockets of these mice. Blood from untreated, healthy mice was used as a control.

## 2.23 Histology staining

On the 15th day of treatment, tumor-bearing mice were euthanized, and the tumors were removed, fixed in 10% neutral buffered formalin, and then embedded in paraffin. On the 30th day, the mice were re-dissected, and their tissues were similarly fixed in formalin and paraffin-embedded. Sections of tumors, each 4 μm thick, were stained with hematoxylin and eosin (H&E) and subjected to terminal deoxynucleotidyl transferase-mediated nick end labeling (TUNEL) staining. Normal organs were also sliced into 4 μm sections for H&E staining.

## 2.24 Statistical analysis

Each experiment was repeated a minimum of three times, and the results are presented as mean ± S.D. To determine significant differences between groups, one-way ANOVA followed by Dunnett's post-hoc test was used. Statistical significance was assumed at a value of $^{****}p < 0.0001$, $^{***}p < 0.001$, $^{**}p < 0.01$, $^{*}p < 0.1$, and ns: no significant difference. All data were analyzed using Origin 8.0 and Excel 2016.

# 3 Results and discussion

The synthesis process of $IrO_x$@MPN is illustrated in Figure 1. We first synthesized multi-cage $IrO_x$ NPs using a direct hydrothermal

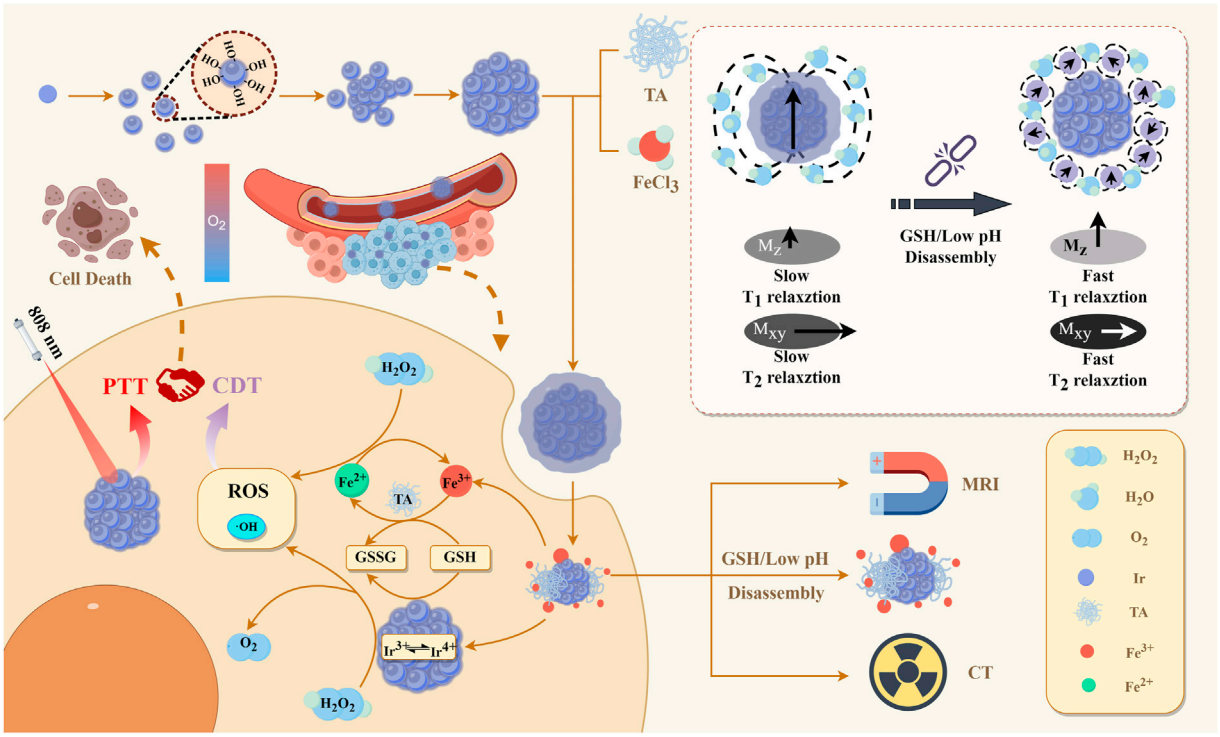


FIGURE 1
Illustration of the fabrication of $IrO_x$@MPN for ($T_1$/$T_2$-weighted) MRI/CT multimodal imaging-guided CDT-PTT synergistic therapy.

method in an alkaline environment by heating $IrCl_3$ at 80°C for 13 h. In the alkaline solution of $IrCl_3$, $[Ir(OH)_6]^{3-}$ initially forms, and upon heating to 80°C, iridium oxide nanoparticles gradually appear. Due to the thermal motion effect under heating conditions, smaller iridium oxide nanoparticles gradually self-aggregate into larger clusters, and after 13 h of continuous reaction, multi-cage $IrO_x$ NPs are obtained. Subsequently, by adding TA and $FeCl_3$ to the weakly alkaline solution of $IrO_x$ NPs, we successfully synthesized $IrO_x$@MPN using a one-step method. Initially, the multi-caged $IrO_x$ nanoparticles with a spherical shape were synthesized through the direct thermal hydrolysis of IrCl3 in an alkaline environment, as exhibited in Figure 2A. The TEM images of $IrO_x$@MPN clearly show a translucent shadow surrounding the $IrO_x$ NPs, confirming the successful encapsulation of the MPN shell (Figure 2B). The XRD pattern of the synthesized $IrO_x$ reveals a broad peak, which is attributed to the limitations of XRD for detecting small particles. (Figure 2C). The XPS spectrum indicates that $IrO_x$ nanoparticles contain not only Ir and O elements but also foreign C and Cl elements from the raw materials (Figure 2D). The deconvolution of the XPS spectrum for the Ir 4f region of $IrO_x$ reveals two binding peaks around 61.8 eV and 64.8 eV, corresponding to $Ir^{4+}$, and peaks at approximately 62.4 eV and 65.6 eV, corresponding to $Ir^{3+}$ (Figure 2E) (Wang D. et al., 2019). In the O 1s region, deconvoluted peaks at about 530.8 eV and 531.7 eV suggest the presence of iridium oxide and hydroxide, respectively (Figure 2F) (Zhang et al., 2013). Next, $FeCl_3$ and TA were introduced to form the MPN layer on the surface of the $IrO_x$ nanoparticles. The UV-Vis absorption spectrum of $IrO_x$@MPN shows the merging of the characteristic absorption peaks of MPN and $IrO_x$ nanoparticles (Figure 2G). Elemental mapping of $IrO_x$@MPN reveals the core-shell architecture of the nanoplatform and shows a uniform distribution of Ir, Fe, and O elements (Supplementary Figure S1). This mapping provides additional confirmation that MPN has been effectively applied to the $IrO_x$ surface, thanks to the adhesive properties of polyphenols. $IrO_x$ and $IrO_x$@MPN exhibit good dispersion in water, with hydrodynamic sizes of approximately 157.4 nm and 259.8 nm, respectively (Figure 2H). The larger size observed in the Dynamic Light Scattering (DLS) measurements, compared to the sizes seen in SEM and TEM images, is likely due to swelling or slight aggregation of $IrO_x$ and $IrO_x$@MPN in solution. Additionally, by controlling the Fe/Ir precursor ratio, the two-step synthesis strategy allows the thickness of the MPN layer to be manipulated, thereby influencing the structure, morphology, and Fe content of the nanoplatform (Figure 2I; Supplementary Figure S2).

Reports indicate that MPN is prone to decomposition when exposed to GSH or in acidic environments (Liu et al., 2023). Due to the formation of a stable orange-colored complex between 1,10-phenanthroline and $Fe^{2+}$, with an absorbance peak at 508 nm, it can be utilized for the detection of $Fe^{2+}$ generated from the reduction of $Fe^{3+}$ (Liu et al., 2023). Therefore, we employed this method to investigate the GSH and pH-responsive disassembly behavior of $IrO_x$@MPN by measuring the release of $Fe^{2+}$. As depicted in Figure 3A, the group treated with $IrO_x$@MPN alone showed no significant UV absorption peak. However, a slight increase in absorbance at 508 nm was detected for $IrO_x$@MPN after exposure to GSH. As expected, a significant increase in absorbance intensity at 508 nm was observed when exposed to both acidic conditions and GSH, indicating the significant release of $Fe^{2+}$ from the MPN. The above results confirm the dual-responsive

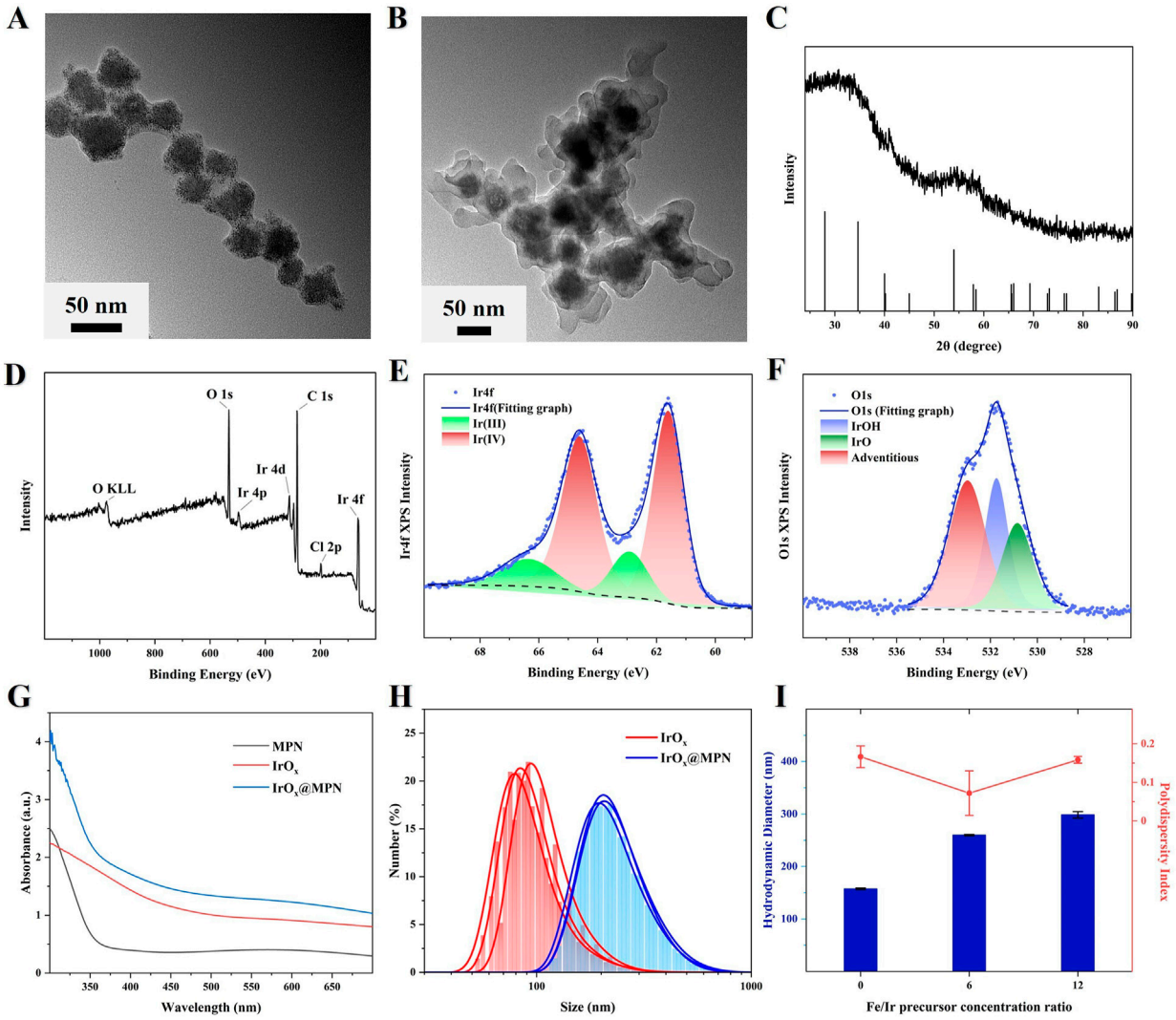


FIGURE 2
**(A,B)** TEM image of $IrO_x$ and $IrO_x$@MPN NPs. **(C)** XRD spectrum of IrOx NPs. **(D)** XPS spectrum of $IrO_x$ NPs. **(E)** Ir 4f XPS spectrum of the $IrO_x$ NPs. **(F)** O 1s XPS spectrum of the $IrO_x$ NPs. **(G)** UV-Vis absorption spectrum of MPN, $IrO_x$ and $IrO_x$@MPN in aqueous solution. **(H)** Hydrodynamic diameter of $IrO_x$ NPs and $IrO_x$@MPN NPs. **(I)** Hydrodynamic diameter and polydispersity index with the different Fe/Ir precursor concentration ratios.

disassembly behavior of the MPN shell. This phenomenon is mainly because the phenolic hydroxyl groups of TA form strong coordination interactions with metal ions under neutral or alkaline conditions, whereas acidic conditions induce protonation of the hydroxyl groups of TA, resulting in weakened metal-phenol coordination (Liu et al., 2023). Additionally, the release of $Fe^{3+}$ from $IrO_x$@MPN in the presence of GSH is linked to the reduced coordination bonds, which occur because $Fe^{3+}$ is reduced. It is important to note that, unlike traditional metal ion-coated nanoparticles, the dual-responsive decomposition of MPN maximizes the utilization efficiency of metal ions (Wang et al., 2022). Subsequently, the enclosed $IrO_x$ are exposed, thereby unleashing the multi-enzyme mimetic functionalities, and providing another reaction pathway for CDT. DTNB, with a maximum absorbance of 408 nm, was used as an indicator to assess the GSH depletion ability of $IrO_x$ and $IrO_x$@MPN. Figure 3B demonstrates that the characteristic absorbance peak of GSH + DTNB at 408 nm is prominently observed. In contrast, the absorbance at this wavelength decreases in the $IrO_x$@MPN-treated groups, signifying effective GSH consumption by $IrO_x$@MPN. Over time, there is a marked reduction in the absorption intensity at 408 nm. This decline occurs because GSH reduces $Fe^{3+}$, and simultaneously, the iridium ions in $IrO_x$@MPN deplete GSH through a cyclic valence change mechanism (Figure 3C). Subsequently, we detected the release of $Fe^{3+}$ from $IrO_x$@MPN under different conditions using 1,10-phenanthroline. It was observed that both GSH and acidic conditions led to the degradation of the MPN shell and the release of $Fe^{3+}$. Moreover, under the combined effect of both conditions, the release rate of $Fe^{3+}$ from the MPN shell significantly increased, demonstrating the dual-responsive degradation capability of the MPN shell to GSH and acidic conditions (Figure 3D). Furthermore, TEM images of $IrO_x$@MPN treated under GSH and acidic conditions confirm the degradation of the MPN shell (Supplementary Figure S2). The

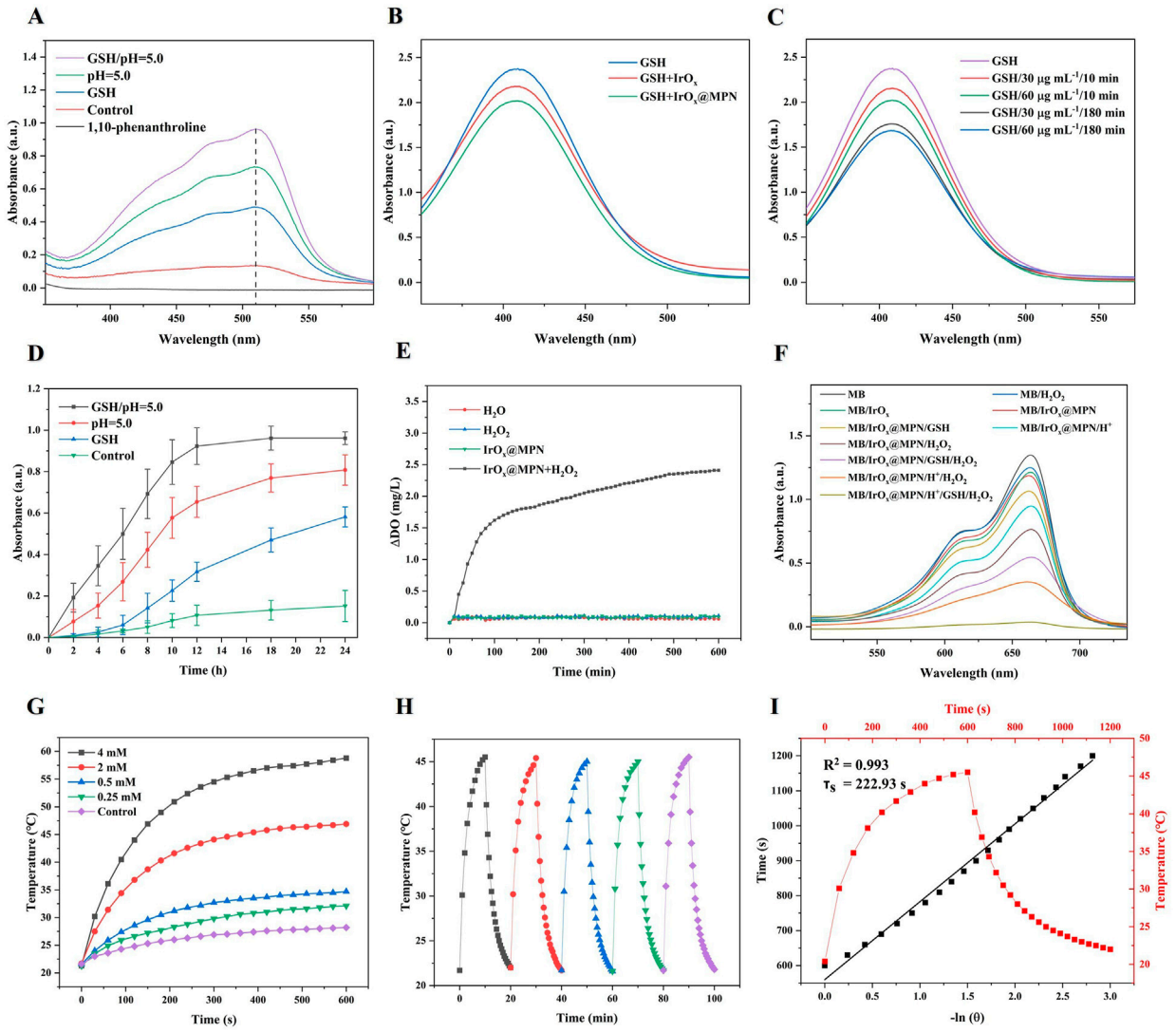


FIGURE 3
**(A)** UV−Vis spectra of pure 1,10-phenanthroline and the mixture of 1,10-phenanthroline and $IrO_x$@MPN with or without GSH or $H^+$. **(B)** GSH depletion (1 mM) under the reduction of $IrO_x$ and $IrO_x$@MPN aqueous solution (50 μg/mL). **(C)** GSH depletion (1 mM) under the reduction of different concentrations (30, 60 μg/mL) and different times (10, 180 min) of $IrO_x$@MPN. **(D)** Time-dependent absorbance at 510 nm for the detection of Fe (III) released using 1,10-phenanthroline under different conditions. **(E)** $O_2$ generation of $IrO_x$@MPN NPs with $H_2O_2$ (100 μM). **(F)** UV−Vis absorption spectra of MB solution treated with different groups. **(G)** Temperature variation of $IrO_x$@MPN NPs aqueous solutions with different concentrations over 10 min irradiation (1.0 W/cm$^2$). **(H)** Heating curve of $IrO_x$@MPN NPs aqueous solution (0.5 mg/mL) for five cycles under irradiation of 808 nm laser (1.0 W/cm$^2$). **(I)** The time constant for heat transfer from the system was determined to be $\tau_s$ = 222.93 s by applying the linear time data from the cooling period (after 10 min) versus negative natural logarithm of the driving force temperature obtained from the cooling stage.

significant GSH consumption by $IrO_x$@MPN helps to reduce the quenching of ROS effectively. The synthesized $IrO_x$@MPN demonstrated catalase-like activity, as evidenced by the detection of dissolved oxygen (DO) following the addition of $H_2O_2$ to the $IrO_x$@MPN solution (Figure 3E). To assess the capability of $IrO_x$@MPN for ·OH generation, methylene blue (MB) was used as an indicator, since ·OH can degrade MB. Figure 3F illustrates the variations in MB degradation across different experimental groups. Compared with the individual $IrO_x$@MPN with $H_2O_2$, the solution containing $IrO_x$@MPN + $H^+$+GSH + $H_2O_2$ exhibits the most pronounced decrease in the absorption peak at 664 nm. This suggests that the ability of $IrO_x$@MPN to generate ·OH is significantly enhanced under GSH and acidic conditions. The above experimental results indicate the remarkable GSH depletion ability and the high Fenton reaction activity of $IrO_x$@MPN through acid and GSH response. Furthermore, owing to its distinctive multi-caged structure, $IrO_x$ exhibits a larger specific surface area, leading to a higher photothermal conversion efficiency of $IrO_x$@MPN. The photothermal performance of $IrO_x$@MPN was evaluated by recording the temperature changes in its aqueous solutions, which were subjected to 808 nm laser irradiation, using a digital thermometer. The results revealed that the photothermal effect increased with concentration (Figure 3G). Specifically, the temperature of a 4 mM $IrO_x$@MPN solution rose to 58.8°C within 10 min of exposure to a 1.0 W/cm$^2$ laser. Additionally, $IrO_x$@MPN, which demonstrates strong thermal stability

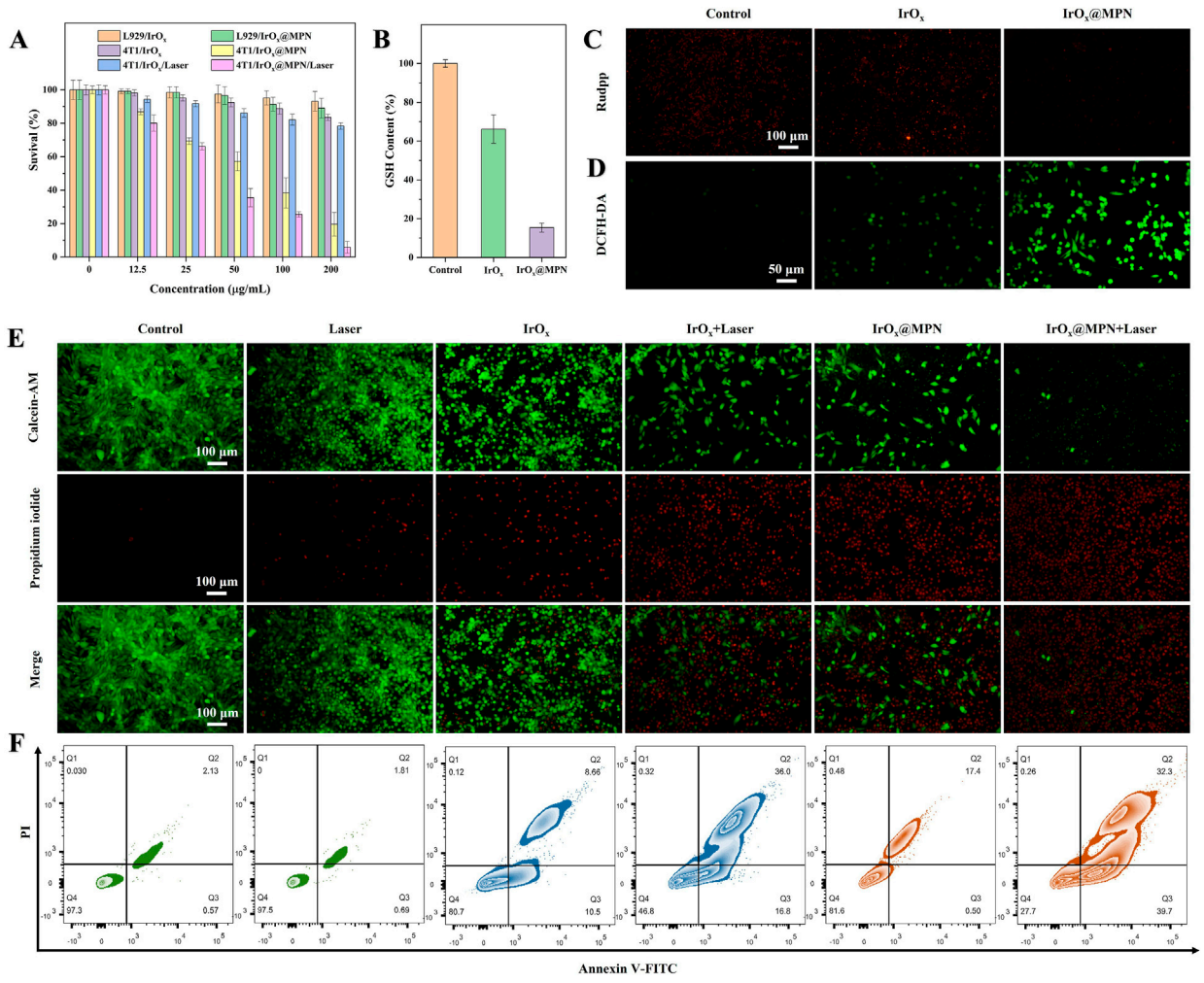


FIGURE 4
**(A)** Survival rate of different cells incubated with different groups for 24 h **(B)** GSH content of 4T1 cells with or without incubation with $IrO_x$ and $IrO_x$@MPN. **(C)** Fluorescent images of 4T1 cells in various groups and stained by Rudpp. **(D)** Fluorescent images of 4T1 cells in various groups and stained by DCFH-DA. **(E)** Calcein-AM/PI staining images of 4T1 cells after different treatments. **(F)** Flow cytometry analysis on the apoptosis levels of 4T1 cells treated with different formulations.

(Figure 3H), has a photothermal conversion efficiency of 60.78% (Figure 3I), which is higher than the reported iridium-based nanomaterials and the majority of photothermal nanomaterials (Zhen et al., 2020b; Li et al., 2017; Ji et al., 2016; Yong et al., 2015).

Since effective cellular uptake is essential for achieving a strong therapeutic effect, $IrO_x$@MPN was labeled with Fluorescein Isothiocyanate Isomer I (FITC) to track its intracellular absorption. As depicted in Supplementary Figure S3, a distinct green fluorescence was observed in 4T1 cells, indicating successful uptake of the nanomaterials. At the 1 h observation point, the cellular uptake of $IrO_x$@MPN reached a plateau. We observed a comparable cellular uptake of $IrO_x$@MPN to that of standalone $IrO_x$, indicating that the MPN shell coating does not affect cellular uptake. The CCK-8 assay was employed to evaluate the cytotoxicity of $IrO_x$@MPN, as illustrated in Figure 4A. $IrO_x$@MPN displayed no noticeable toxicity to mouse fibroblasts (L929 cells), even at elevated concentrations. At 200 μg/mL, cell viability remained at 89.0%, indicating that $IrO_x$@MPN exhibits favorable biocompatibility. Due to the inhibitory effect of excessive GSH in the TME on the therapeutic efficacy of ROS generation during CDT, we employed a reduced GSH assay kit to further evaluate the GSH consumption capability of $IrO_x$@MPN. This process was crucial in understanding the potential of $IrO_x$@MPN to overcome the GSH-mediated resistance in CDT. Figure 4B illustrates that GSH levels in the $IrO_x$@MPN group were significantly reduced relative to both the control group and the $IrO_x$ group. This result corroborates the DTNB degradation assay findings, highlighting the capability of $IrO_x$@MPN to effectively reduce intracellular GSH levels. In 4T1 cells, $IrO_x$@MPN could efficiently convert $H_2O_2$ into $O_2$, resulting in almost complete quenching of the fluorescence of the oxygen probe [Ru $(DPP)_3$] $Cl_2$ (Rudpp) in comparison to cells treated with $IrO_x$ or PBS (Figure 4C). 2′,7′-dichlorofluorescin diacetate (DCFH-DA) is employed to measure the levels of ROS level in cells. Figure 4D demonstrates that 4T1 cells treated with $IrO_x$@MPN displayed notably more intense green fluorescence compared to both the control and $IrO_x$ groups. This suggests that the increase in intracellular oxygen level will enhance the production of ROS in

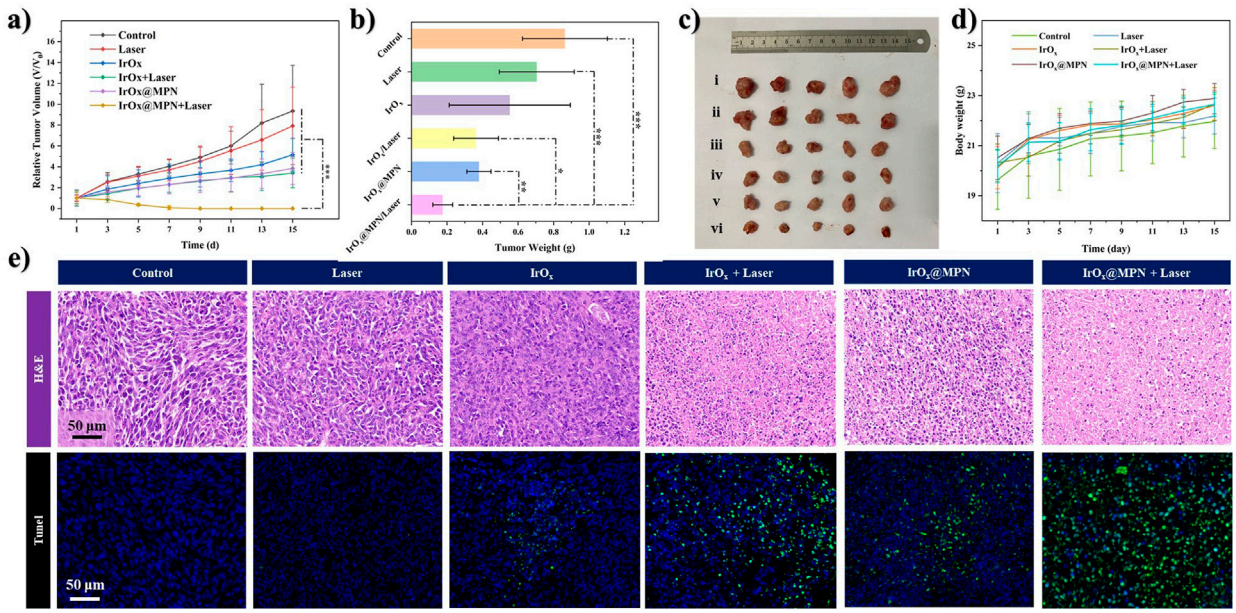


FIGURE 5
**(A)** Relative tumor growth trend curves of mice treated with different formulations (n = 5, $*p < 0.05$, $**p < 0.01$, $***p < 0.001$). **(B)** The average tumor mass in mice sacrificed after 14 days observation. $*p < 0.05$, $**p < 0.01$, $***p < 0.001$. **(C)** The digital photos of excised tumors in different groups after 14 days of treatment (i. Control; ii. Laser; iii. $IrO_x$; iv. $IrO_x$ + Laser; v. $IrO_x$@MPN; vi. $IrO_x$@MPN + Laser). **(D)** Variation of body weights of tumor-bearing mice with different treatments. **(E)** 4T1 tumor tissues stained with H&E, TUNEL (cell nuclei were stained with DAPI) in different groups.

cancer cells to some extent. It may be attributed to the differential GSH consumption capacity between $IrO_x$ and $IrO_x$@MPN, along with the presence of $Fe^{2+}$ in $IrO_x$@MPN. Although both $IrO_x$ and $IrO_x$@MPN can deplete GSH and generate ROS, the enhanced GSH consumption capability of $IrO_x$@MPN is more effective in disrupting the intracellular redox balance. Additionally, $IrO_x$@MPN has the ability to induce ROS production through dual pathways simultaneously. Consequently, $IrO_x$@MPN exhibits a stronger CDT effect compared with $IrO_x$. This result was confirmed in the dual staining experiment with calcein-AM and PI (Figure 4E). Without laser irradiation, the $IrO_x$@MPN group showed a considerable increase in cell death compared to both the control and $IrO_x$ groups. With 808 nm laser exposure, the combination of CDT and PTT resulted in almost complete cell death, underscoring the immense potential of $IrO_x$@MPN as an effective strategy for CDT/PTT. Additionally, cell apoptosis was analyzed by employing the Annexin V-FITC and PI dual staining technique. Flow cytometry was employed to confirm the enhanced therapeutic efficacy of the combined CDT/PTT approach (Figure 4F). Initially, without laser irradiation, apoptosis rates in cells exposed to $IrO_x$@MPN were notably higher (19.16%) compared to the control group (2.7%). After 10 min of 808 nm laser exposure, the $IrO_x$@MPN/Laser group exhibited a marked increase in 4T1 cell apoptosis (72.0%), significantly surpassing the rates observed in both the control group (2.5%) and the $IrO_x$ group (52.8%). Under the dual-responsive conditions of acidity and GSH, $IrO_x$@MPN achieves more effective CDT by disrupting the GSH-mediated cellular ADS and inducing ROS production through dual pathways. When combined with PTT, the apoptosis of cancer cells could be effectively achieved.

Based on the promising *in vitro* results, we developed 4T1 tumor models in mice to assess the effectiveness of $IrO_x$@MPN in inhibiting tumor growth *in vivo*. The mice were randomly assigned to six different groups: Control, Laser, $IrO_x$ (single-pathway CDT), $IrO_x$ + Laser (single-pathway CDT/PTT), $IrO_x$@MPN (dual-pathway CDT), and $IrO_x$@MPN + Laser (dual-pathway CDT/PTT) 24 h after intravenous injection. In the laser-treated groups, tumors were exposed to 808 nm laser irradiation for 10 min at a power density of 1.0 W/cm$^2$. Throughout the 15-day treatment period, tumor size and body weight were measured every 2 days (Figure 5A). The tumors in the $IrO_x$@MPN + Laser group showed significant suppression, whereas tumors in the other groups did not exhibit similar effects (Figures 5B–D). To assess the antitumor activity of $IrO_x$@MPN at a tissue level, tumor sections were subjected to histological staining (Figure 5E). The H&E staining results revealed that tumors treated with $IrO_x$@MPN + Laser exhibited the most pronounced karyolysis and plasmatorrhexis. Furthermore, the TUNEL staining images of tumor sections from the IrOx@MPN + Laser group displayed the most intense green fluorescence, indicating a significant degree of tumor inhibition. The above results proved that $IrO_x$@MPN showed a significant therapeutic effect in the combination therapy of CDT and PTT by enhancing GSH consumption and dual-pathway ROS generation. Throughout the treatment period, no significant variations in body weight were detected among the experimental and control groups. (Figure 5D). Additionally, no significant tissue damage was observed in the primary organs of mice treated with $IrO_x$@MPN (Supplementary Figure S4). Hematology analysis showed no significant difference between $IrO_x$@MPN and the control group (Supplementary Figure S5), further confirming the satisfactory biosafety of the $IrO_x$@MPN nanoplatform.

10.3389/fchem.2024.1475131

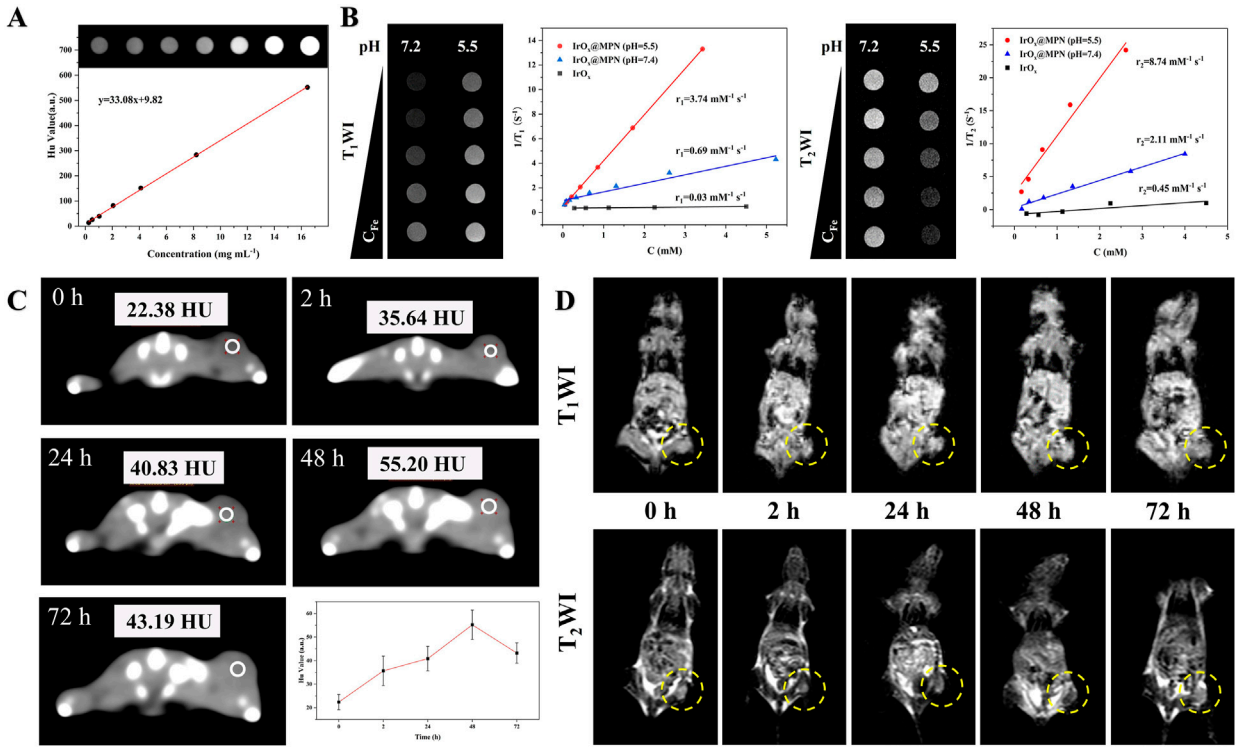


FIGURE 6
Multi-model imaging effects of $IrO_x$@MPN NPs. **(A)** *In vitro* computed tomography signals of $IrO_x$@MPN NPs with different concentrations. **(B)** Plots of $1/T_1$ and $1/T_2$ over the concentrations of Fe from $IrO_x$@MPN NPs. **(C)** *In vivo* computed tomography images of Balb/C mice pre- and post-intravenously injected with 100 μL of $IrO_x$@MPN (3 mg/mL in saline). **(D)** *In vivo* $T_1/T_2$ weighted MRI photos of tumor-bearing mouse after intravenous injection of $IrO_x$@MPN NPs (100 μL, 2 mg/mL in saline) at various time intervals.

Considering the excellent X-ray absorption capability of Ir, we investigated the *in vitro* CT imaging capability of $IrO_x$@MPN. As illustrated in Figure 6A, a strong linear relationship was observed between Hounsfield units (HU) and Ir concentration, with a calculated X-ray attenuation coefficient of 33.08 HU·mL/mg for $IrO_x$@MPN, which is higher than clinical iodine-based contrast agent (16.4 HU·mL/mg). Moreover, since $Fe^{2+}$ and $Fe^{3+}$ possess multiple unpaired electrons, $IrO_x$@MPN can serve as an MRI contrast agent theoretically. As shown in Figure 6B, the $T_1$ and $T_2$ signal of $IrO_x$@MPN gradually increased with increasing Fe concentration. The values of longitudinal relaxivity ($r_1$) and transverse relaxivity ($r_2$) values were measured at 0.69 mM/s and 2.11 mM/s, respectively. At pH 5.5, the signal contrast on both $T_1$WI and $T_2$WI of $IrO_x$@MPN is enhanced, particularly in $T_2$WI. The $r_1$ and $r_2$ relaxation rates increase to 3.74 mM/s and 8.74 mM/s, respectively. To further assess its potential as an *in vivo* multimodal CT and MR imaging contrast agent, we intravenously injected $IrO_x$@MPN into 4T1 tumor-bearing mice and performed CT and MRI scans at several intervals (0 h, 2 h, 24 h, 48 h). After intravenous administration, effective accumulation of $IrO_x$@MPN at the tumor site was noted, attributed to the EPR effect. CT images revealed significant enhancement in visual contrast at 24 h after injection, reaching a peak at 48 h, with an increase from 22.38 HU to 55.20 HU (Figure 6C). For $T_1$WI and $T_2$WI, distinct differences in signal intensity were observed between the tumor region and surrounding normal tissues, with the optimal effect reached at 48 h post-injection (Figure 6D). These results demonstrate that $IrO_x$@MPN, with its exceptional capabilities, is an excellent candidate for use as a contrast agent in both CT and MRI ($T_1/T_2$) multimodal imaging.

## 4 Conclusion

In summary, we constructed a versatile nanoplatform ($IrO_x$@MPN) consisting of an $IrO_x$ core and self-assembled MPN based on $Fe^{3+}$ and TA. This nanoplatform could respond to GSH and pH in the TME. This dual responsiveness sets the foundation for a powerful CDT, showcasing its potential in cancer treatment. The MPN shell composed of $Fe^{3+}$ and TA, could undergo responsive disassembly in the TME. The valence state cycling of $Fe^{3+}/Fe^{2+}$ and $Ir^{4+}/Ir^{3+}$ through GSH consumption disrupts the ADS, leading to a redox imbalance and significantly enhancing the Fe- and Ir-mediated Fenton and Fenton-like reaction, thus achieving a remarkable dual-pathway CDT. Simultaneously, the high photothermal conversion efficiency of iridium-based nanomaterials and the unique multi-cage structure of $IrO_x$ endow $IrO_x$@MPN with a powerful PTT capability. Additionally, the presence of Ir and iron ions in $IrO_x$@MPN grants it excellent CT and MRI ($T_1/T_2$) multimodal imaging capabilities, making it a promising diagnostic tool for tumor diagnosis. As a result, $IrO_x$@MPN, as an easy-to-synthesize nanoplatform, achieves dual-pathways CDT combined PTT on the basis of degradation in response to acidic microenvironment and GSH. It also possesses

stable multimodal imaging capabilities, holding immense potential in early cancer diagnosis, treatment, and therapeutic response monitoring. This study provides a feasible strategy for constructing an integrated nanoplatform with dual responsiveness for the diagnosis and treatment of TME, showing promising potential for future development.

## Data availability statement

The original contributions presented in the study are included in the article/Supplementary Material, further inquiries can be directed to the corresponding authors.

## Ethics statement

The animal study was approved by all the animal experiments were conducted following the National Regulation of China for Care and Use of Laboratory Animals and approved by the Institutional Animal Care and Use Committee of Changchun Institute of Applied Chemistry, Chinese Academy of Sciences (Grant no. 20230065). The study was conducted in accordance with the local legislation and institutional requirements.

## Author contributions

RM: Data curation, Investigation, Methodology, Writing–original draft. PZ: Data curation, Formal Analysis, Methodology, Resources, Writing–review and editing. XC: Software, Validation, Visualization, Writing–review and editing. MZ: Software, Validation, Visualization, Writing–review and editing. QH: Conceptualization, Methodology, Project administration, Supervision, Writing–review and editing. QY: Conceptualization, Funding acquisition, Project administration, Supervision, Writing–review and editing.

## Funding

The author(s) declare that financial support was received for the research, authorship, and/or publication of this article. This research was funded by Jilin Province Science and Technology Department, grant number 20230204098YY and 20210101197JC.

## Conflict of interest

The authors declare that the research was conducted in the absence of any commercial or financial relationships that could be construed as a potential conflict of interest.

## Publisher's note

All claims expressed in this article are solely those of the authors and do not necessarily represent those of their affiliated organizations, or those of the publisher, the editors and the reviewers. Any product that may be evaluated in this article, or claim that may be made by its manufacturer, is not guaranteed or endorsed by the publisher.

## Supplementary material

The Supplementary Material for this article can be found online at: https://www.frontiersin.org/articles/10.3389/fchem.2024.1475131/full#supplementary-material

## References

Abbas, M., Zou, Q., Li, S., and Yan, X. (2017). Self-assembled peptide- and protein-based nanomaterials for antitumor photodynamic and photothermal therapy. *Adv. Mater* 29, 1605021. doi:10.1002/adma.201605021

An, B., and Tc, Z. (2002). Fabrication of anodically electrodeposited iridium oxide film pH microelectrodes for microenvironmental studies. *Anal. Chem.* 74, 5726–5733. doi:10.1021/ac020326l

Cen, D., Zheng, Q., Zheng, B., Zhou, R., Xiao, X., Zhang, T., et al. (2023). A near-infrared light-responsive ROS cascade nanoplatform for synergistic therapy potentiating antitumor immune responses. *Adv. Funct. Mater* 33, 2211402. doi:10.1002/adfm.202211402

Deng, X., Zhao, R., Song, Q., Zhang, Y., Zhao, H., Hu, H., et al. (2022). Synthesis of dual-stimuli responsive metal organic framework-coated iridium oxide nanocomposite functionalized with tumor targeting albumin-folate for synergistic photodynamic/photothermal cancer therapy. *Drug Deliv.* 29, 3142–3154. doi:10.1080/10717544.2022.2127973

Feng, L., Liu, B., Xie, R., Wang, D., Qian, C., Zhou, W., et al. (2021). An ultrasmall $SnFe_2O_4$ nanozyme with endogenous oxygen generation and glutathione depletion for synergistic cancer therapy. *Adv. Funct. Mater* 31, 2006216. doi:10.1002/adfm.202006216

Getachew, G., Korupalli, C., Rasal, A. S., and Chang, J.-Y. (2021). ROS generation/scavenging modulation of carbon dots as phototherapeutic candidates and peroxidase mimetics to integrate with polydopamine nanoparticles/$GO_x$ towards cooperative cancer therapy. *Compos. Part B Eng.* 226, 109364. doi:10.1016/j.compositesb.2021.109364

Guo, J., Ping, Y., Ejima, H., Alt, K., Meissner, M., Richardson, J. J., et al. (2014). Engineering multifunctional capsules through the assembly of metal–phenolic networks. *Angew. Chem. Int. Ed.* 53, 5546–5551. doi:10.1002/anie.201311136

Hao, Y., Dong, Z., Chen, M., Chao, Y., Liu, Z., Feng, L., et al. (2020). Near-infrared light and glucose dual-responsive cascading hydroxyl radical generation for *in situ* gelation and effective breast cancer treatment. *Biomaterials* 228, 119568. doi:10.1016/j.biomaterials.2019.119568

Huang, X., Zhang, W., Guan, G., Song, G., Zou, R., and Hu, J. (2017). Design and functionalization of the NIR-responsive photothermal semiconductor nanomaterials for cancer theranostics. *Accounts Chem. Res.* 50, 2529–2538. doi:10.1021/acs.accounts.7b00294

Jana, D., and Zhao, Y. (2022). Strategies for enhancing cancer chemodynamic therapy performance. *Exploration* 2, 20210238. doi:10.1002/EXP.20210238

Ji, M., Xu, M., Zhang, W., Yang, Z., Huang, L., Liu, J., et al. (2016). Structurally well-defined Au@$Cu_{2-x}S$ core–shell nanocrystals for improved cancer treatment based on enhanced photothermal efficiency. *Adv. Mater.* 28, 3094–3101. doi:10.1002/adma.201503201

Jiang, F., Ding, B., Liang, S., Zhao, Y., Cheng, Z., Xing, B., et al. (2021). Intelligent $MoS_2$–CuO heterostructures with multiplexed imaging and remarkably enhanced antitumor efficacy via synergetic photothermal therapy/chemodynamic therapy/immunotherapy. *Biomaterials* 268, 120545. doi:10.1016/j.biomaterials.2020.120545

Li, B., Wang, X., Wu, X., He, G., Xu, R., Lu, X., et al. (2017). Phase and morphological control of $MoO_{3-x}$ nanostructures for efficient cancer theragnosis therapy. *Nanoscale* 9, 11012–11016. doi:10.1039/C7NR03469E

Li, X., Lovell, J. F., Yoon, J., and Chen, X. (2020). Clinical development and potential of photothermal and photodynamic therapies for cancer. *Nat. Rev. Clin. Oncol.* 17, 657–674. doi:10.1038/s41571-020-0410-2

Lin, L., Wang, S., Deng, H., Yang, W., Rao, L., Tian, R., et al. (2020). Endogenous labile iron pool-mediated free radical generation for cancer chemodynamic therapy. *J. Am. Chem. Soc.* 142, 15320–15330. doi:10.1021/jacs.0c05604

Lin, L.-S., Huang, T., Song, J., Ou, X.-Y., Wang, Z., Deng, H., et al. (2019). Synthesis of copper peroxide nanodots for $H_2O_2$ self-supplying chemodynamic therapy. *J. Am. Chem. Soc.* 141, 9937–9945. doi:10.1021/jacs.9b03457

Liu, Y., Bhattarai, P., Dai, Z., and Chen, X. (2019). Photothermal therapy and photoacoustic imaging via nanotheranostics in fighting cancer. *Chem. Soc. Rev.* 48, 2053–2108. doi:10.1039/c8cs00618k

Liu, Y., Zhen, W., Jin, L., Zhang, S., Sun, G., Zhang, T., et al. (2018). All-in-One theranostic nanoagent with enhanced reactive oxygen species generation and modulating tumor microenvironment ability for effective tumor eradication. *ACS Nano* 12, 4886–4893. doi:10.1021/acsnano.8b01893

Liu, Z., Liu, S., Liu, B., Bian, Y., Yuan, M., Yang, C., et al. (2023). Fe(III)-Naphthazarin metal-phenolic networks for glutathione-depleting enhanced ferroptosis-apoptosis combined cancer therapy. *Small* 19, e2207825. doi:10.1002/smll.202207825

Manivasagan, P., Joe, A., Han, H.-W., Thambi, T., Selvaraj, M., Chidambaram, K., et al. (2022). Recent advances in multifunctional nanomaterials for photothermal-enhanced Fenton-based chemodynamic tumor therapy. *Mater Today Bio* 13, 100197. doi:10.1016/j.mtbio.2021.100197

Meng, X., Zhang, X., Liu, M., Cai, B., He, N., and Wang, Z. (2020). Fenton reaction-based nanomedicine in cancer chemodynamic and synergistic therapy. *Appl. Mater. Today* 21, 100864. doi:10.1016/j.apmt.2020.100864

Nie, T., Zou, W., Meng, Z., Wang, L., Ying, T., Cai, X., et al. (2022). Bioactive iridium nanoclusters with glutathione depletion ability for enhanced sonodynamic-triggered ferroptosis-like cancer cell death. *Adv. Mater* 34, 2206286. doi:10.1002/adma.202206286

Peng, M., Ju, E., Xu, Y., Wang, Y., Lv, S., Shao, D., et al. (2022). Dual-responsive disassembly of core-shell nanoparticles with self-supplied $H_2O_2$ and autocatalytic Fenton reaction for enhanced chemodynamic therapy. *Npg Asia Mater* 14, 95–13. doi:10.1038/s41427-022-00447-8

Shen, J., Rees, T. W., Ji, L., and Chao, H. (2021). Recent advances in ruthenium(II) and iridium(III) complexes containing nanosystems for cancer treatment and bioimaging. *Coord. Chem. Rev.* 443, 214016. doi:10.1016/j.ccr.2021.214016

Spinello, A., Bonsignore, R., Barone, G., Keppler, B. K., and Terenzi, A. (2016). Metal ions and metal complexes in alzheimer's disease. *Curr. Pharm. Des.* 22, 3996–4010. doi:10.2174/1381612822666160520115248

Tang, Z., Zhao, P., Wang, H., Liu, Y., and Bu, W. (2021). Biomedicine meets Fenton Chemistry. *Chem. Rev.* 121, 1981–2019. doi:10.1021/acs.chemrev.0c00977

Wang, D., Li, Q., Han, C., Lu, Q., Xing, Z., and Yang, X. (2019c). Atomic and electronic modulation of self-supported nickel-vanadium layered double hydroxide to accelerate water splitting kinetics. *Nat. Commun.* 10, 3899. doi:10.1038/s41467-019-11765-x

Wang, X., Zhong, X., Lei, H., Geng, Y., Zhao, Q., Gong, F., et al. (2019b). Hollow $Cu_2Se$ nanozymes for tumor photothermal-catalytic therapy. *Chem. Mater* 31, 6174–6186. doi:10.1021/acs.chemmater.9b01958

Wang, X., Zhong, X., Zha, Z., He, G., Miao, Z., Lei, H., et al. (2020). Biodegradable $CoS_2$ nanoclusters for photothermal-enhanced chemodynamic therapy. *Appl. Mater Today* 18, 100464. doi:10.1016/j.apmt.2019.100464

Wang, Z., Guo, Y., Fan, Y., Chen, J., Wang, H., Shen, M., et al. (2022). Metal-phenolic-network-coated dendrimer-drug conjugates for tumor MR imaging and chemo/chemodynamic therapy via amplification of endoplasmic reticulum stress. *Adv. Mater* 34, e2107009. doi:10.1002/adma.202107009

Wang, Z., Zhen, X., Upputuri, P. K., Jiang, Y., Lau, J., Pramanik, M., et al. (2019a). Redox-activatable and acid-enhanced nanotheranostics for second near-infrared photoacoustic tomography and combined photothermal tumor therapy. *Acs Nano* 13, 5816–5825. doi:10.1021/acsnano.9b01411

Yin, K., Chao, Y., Lv, F., Tao, L., Zhang, W., Lu, S., et al. (2021). One nanometer PtIr nanowires as high-efficiency bifunctional catalysts for electrosynthesis of ethanol into high value-added multicarbon compound coupled with hydrogen production. *J. Am. Chem. Soc.* 143, 10822–10827. doi:10.1021/jacs.1c04626

Yip, A. M.-H., and Lo, K. K.-W. (2018). Luminescent rhenium(I), ruthenium(II), and iridium(III) polypyridine complexes containing a poly(ethylene glycol) pendant or bioorthogonal reaction group as biological probes and photocytotoxic agents. *Coord. Chem. Rev.* 361, 138–163. doi:10.1016/j.ccr.2018.01.021

Yong, Y., Cheng, X., Bao, T., Zu, M., Yan, L., Yin, W., et al. (2015). Tungsten sulfide quantum dots as multifunctional nanotheranostics for *in vivo* dual-modal image-guided photothermal/radiotherapy synergistic therapy. *ACS Nano* 9, 12451–12463. doi:10.1021/acsnano.5b05825

Zhang, H., Zhang, L., Zhong, H., Niu, S., Ding, C., and Lv, S. (2022). Iridium oxide nanoparticles-based theranostic probe for *in vivo* tumor imaging and synergistic chem/photothermal treatments of cancer cells. *Chem. Eng. J.* 430, 132675. doi:10.1016/j.cej.2021.132675

Zhang, Y., Wu, C., Zhou, X., Wu, X., Yang, Y., Wu, H., et al. (2013). Graphene quantum dots/gold electrode and its application in living cell $H_2O_2$ detection. *Nanoscale* 5, 1816–1819. doi:10.1039/C3NR33954H

Zhen, W., Liu, Y., Lin, L., Bai, J., Jia, X., Tian, H., et al. (2018). BSA-$IrO_2$: catalase-like nanoparticles with high photothermal conversion efficiency and a high X-ray absorption coefficient for anti-inflammation and antitumor theranostics. *Angew. Chem. Int. Ed.* 57, 10309–10313. doi:10.1002/anie.201804466

Zhen, W., Liu, Y., Wang, W., Zhang, M., Hu, W., Jia, X., et al. (2020a). Specific "unlocking" of a nanozyme-based butterfly effect to break the evolutionary fitness of chaotic tumors. *Angew. Chem. Int. Ed.* 59, 9491–9497. doi:10.1002/anie.201916142

Zhen, W., Liu, Y., Zhang, M., Hu, W., Wang, W., Jia, X., et al. (2020b). Multi-caged $IrO_x$ for facile preparation of "six-in-one" nanoagent for subcutaneous and lymphatic tumors inhibition against recurrence and metastasis. *Adv. Funct. Mater* 30, 2002274. doi:10.1002/adfm.202002274

Zheng, N., Fu, Y., Liu, X., Zhang, Z., Wang, J., Mei, Q., et al. (2022). Tumor microenvironment responsive self-cascade catalysis for synergistic chemo/chemodynamic therapy by multifunctional biomimetic nanozymes. *J. Mater Chem. B* 10, 637–645. doi:10.1039/d1tb01891d

Zou, W., Wang, L., Hao, J., Jiang, L., Du, W., Ying, T., et al. (2022). Phase-change cascaded nanomedicine for intensive photothermal-enhanced nanocatalytic therapy via tumor oxidative stress amplification. *Compos Part B-Eng* 234, 109707. doi:10.1016/j.compositesb.2022.109707